ORIGINAL PAPER

A novel approach for slope stability evaluation considering landslide dynamics and its application to reservoir landslide

Ming-liang Chen[1,2,3] · Jia-wen Zhou[2,3] · Xing-guo Yang[2,3]

Abstract

A novel and robust slope stability evaluation method based on energy method and radial slices method (RSM) is proposed and validated in terms of strength parameter sensitivity and determination of the critical sliding surface. The sensitivity analysis shows that the deviation from the limit equilibrium method (LEM) does not exceed 1.5%, demonstrating the feasibility of the proposed method. Different from LEM, the proposed framework gets functional enhancements: (1) This method considers the failure mode of the slope as a combination of translation and rotation, which is more in line with the actual monitoring results; (2) if the virtual displacement is regarded as a variable, the effect of accumulated displacement on slope stability can be studied; (3) if the factor of safety (FOS) for the slope is less than 1, this method can be extended to analyze movement of landslide mass after instability using the energy balance. Then, the proposed framework is applied to the 1963 Vajont event and Xinhua event to analyze the slope stability at the changes of reservoir water level and the dynamics after instability. Comparing slopes with different deformation patterns in calculating stability, the paper finds that permeability is the key to understanding the deformation response and summarizes the failure mechanism. For 1963 Vajont landslide, the proposed framework calculates the maximum velocity of the intermediate section to be 21.51 m/s, which is in general agreement with the inference by Hendron and Patton (Eng Geol 24:475–491, 1987), and superior to Zaniboni and Tinti (Nat Hazards 70:567–592, 2014)'s calculation of less than 20 m/s. Through research and application, the superiority of the proposed framework in analyzing slope hazards is shown.

Keywords Slope stability evaluation · Radial slices method · Energy conservation · Landslide dynamic · Reservoir landslide

---

✉ Ming-liang Chen
2023800025@hfut.edu.cn

1   School of Civil Engineering, Hefei University of Technology, Hefei 230009, Anhui, China

2   State Key Laboratory of Hydraulics and Mountain River Engineering, Sichuan University, Chengdu 610065, China

3   College of Water Resource and Hydropower, Sichuan University, Chengdu 610065, China

1 Introduction

The prediction/failure criterion of landslide is a frontier topic in international engineering geology discipline. The establishment of instability criteria with high prediction success rate is the basis for precise mitigation and emergency avoidance. The most used method to identify landslide instability in engineering practice is threshold warning. As an indicator of slope stability, rain-induced landslides generally use rainfall thresholds for early warning (Guzzetti et al. 2007; 2008), while gravity landslides mainly use deformation thresholds (contain displacement, deformation rate, tangential angle, etc.) for early warning (Fan et al. 2019; Xu et al. 2020). Thanks to the rapid development of computer technology and the increasing maturity of related numerical simulation software, the factor of safety (FOS) is also one of the important bases for determining whether landslide disasters occur. Due to the simple operation and rich engineering application practice, the limit equilibrium method (LEM) is the most used numerical method in calculating slope stability (Fredlund and Krahn 1977; Fredlund et al. 1981). Most of the LEMs consider the static equilibrium conditions and Mohr–Coulomb criterion, and the probability of shear failure is calculated by dividing the geotechnical mass on the sliding surface into a certain number of slices. The finite element method (FEM) can be used to improve the accuracy of the LEM in evaluating the stability of slopes with complex changes in material properties (Liu et al. 2015; Ozbay and Cabalar 2015) by prompting the accuracy of stress state analysis. This way differs from the strength reduction method (SRM) with elasto-plastic analysis and only the FEM. The FEM determines whether the landslide is unstable mainly by determining whether the numerical calculations converge, whether the plastic zone is penetrated, and whether the displacement accumulation curve of the characteristic points changes abruptly. Nowadays, the material point method and the smooth particle dynamics method have become the frontier methods to study the slope stability. The material point method is used by discretizing the continuum and then focusing the mass, velocity and stress properties of each sub-mass on the Lagrangian point (Bandara et al. 2016; Wang et al. 2018). The smooth particle hydrodynamics method is a network-free technique that uses the Lagrangian method to replace the interacting masses with a continuous flow mass (Girardi et al. 2022; Ma et al. 2022). Infinite slope theory is often used to evaluate the probability of rainfall-induced landslides in a large area. Because of the large aspect ratio, infinite slope theory simplifies slope stability analysis by assuming that shear failure occurs along a sliding surface parallel to the slope direction. Building on the concept of effective stress in unsaturated soils by Lu and Likos (2006), Lu and Godt (2008) developed a general analytical framework for assessing the stability of infinite slopes with sliding surfaces above the water table. Qi and Vanapalli (2015; 2016) further discussed the strain softening behavior of unsaturated soils for the effect of shallow slope failure. At present, with the emergence of artificial intelligence technology, how to apply new methods to improve the effectiveness of slope stability evaluation has become a hot spot (Lin et al. 2022; Wang et al. 2023).

In summary, although researchers have been developing new methods in landslide instability criterion/prediction forecasting research, the breakthrough of research results in engineering application practice is still very slow. This is because landslide hazards are not induced by a single factor, but are the result of the joint action of many unfavorable factors. Landslides with different material compositions (clay, rock, gravelly soil, etc.), different scales (from m^3 level to 10^9 m^3 level), and different genesis types vary greatly in their deformation characteristics (including the cumulative threshold of displacement before destabilization) as shown in Fig. 1. For deformation threshold warning, the most
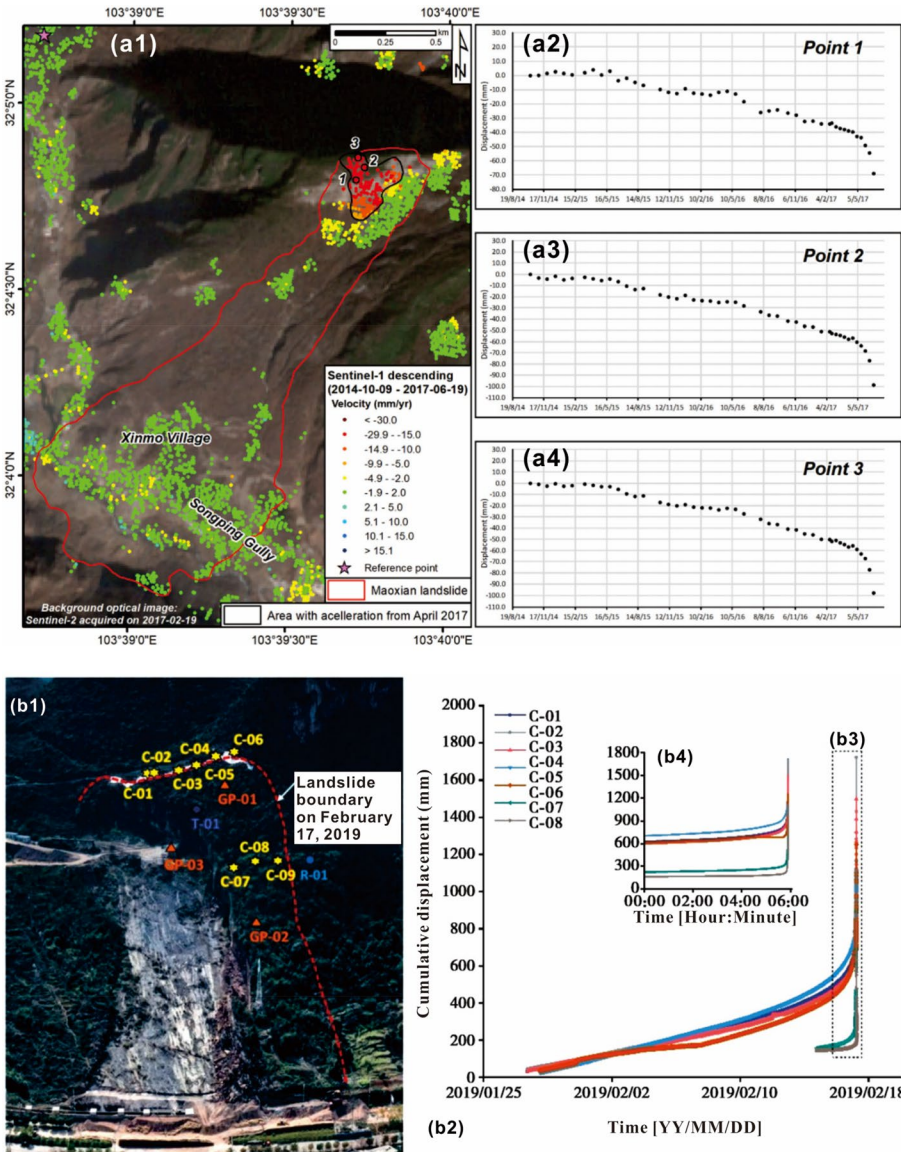
Fig. 1 Deformation accumulation characteristics of typical landslide events: **a** the 2017 June 24 Maoxian event (Intrieri et al. 2018; Carlà et al. 2019); **b** the 2019 February 17 Longjing event (Fan et al. 2019); **c** the 1963 Vajont event (Paronuzzi et al. 2016); and **d** the Xinhua event (Chen et al. 2018)

appropriate indicator is the tangential angle of the displacement accumulation curve. It reflects the transition of landslides from slow creep to high velocity motion. However, this course is usually very short, and how to develop an emergency response plan based on the trend of the tangential angle becomes the top priority of this research direction. When numerical simulations are used to determine landslide occurrence, the traditional methods have their own shortcomings: (1) The infinite slope theory simplifies the slope morphology
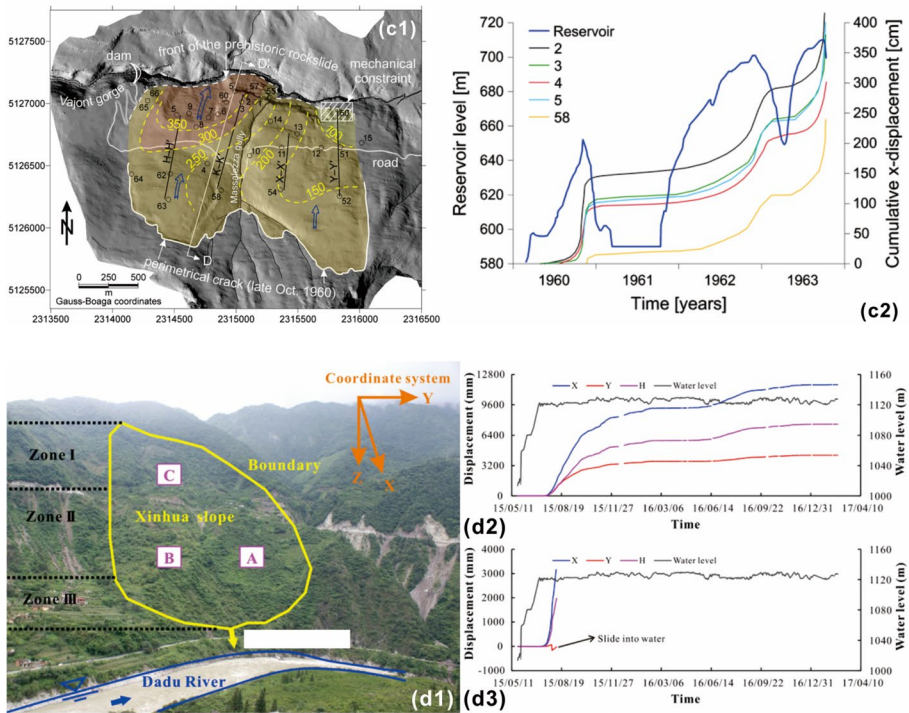
Fig. 1 (continued)

and is not applicable to the evaluation of single site; (2) the LEM suffers from an imperfect theoretical basis and the assumption that landslides are regarded as rigid masses; and (3) the FEM deals with large deformations of slopes in such a way that the model mesh can be severely deformed or even fail. In addition, although the material point method and the smooth particle dynamics method have their own strong advantages and broad application prospects, they are very expensive to handle in the computational process and far from commercial application, and still need to be developed by scholars in related fields. In addition, the extensive experience gained in practical applications of the LEM over the past century has made it the most popular, acceptable and reliable technique. Many off-the-shelf commercial codes are based on various two-dimensional (2D) LEMs, such as slope/W (GeoSlope International Ltd., 2007) and SVSlope (Fredlund 2009).

However, the monitoring results of some case slopes show the limitations of traditional LEM. First, when using the LEM, the movement of landslide mass is characterized by the set of translational movements of slices along the sliding surface. Li et al. (2020) found by terrestrial laser scanning that the development of landslide hazards is characterized by a composite failure pattern for a slope, including translation and rotation. Second, in fact, a slope that is considered stable by both external morphological observation and monitoring results is not absolute stationary, as shown in Fig. 2a. The rising-drawdown cycles of water level produce minor disturbances on the deposits of the Mogangling slope. The same hydrodynamic conditions produced large deformations on the deposits of another Xinhua slope of the reservoir as shown in Fig. 2b. Usually, the deformation of Xinhua
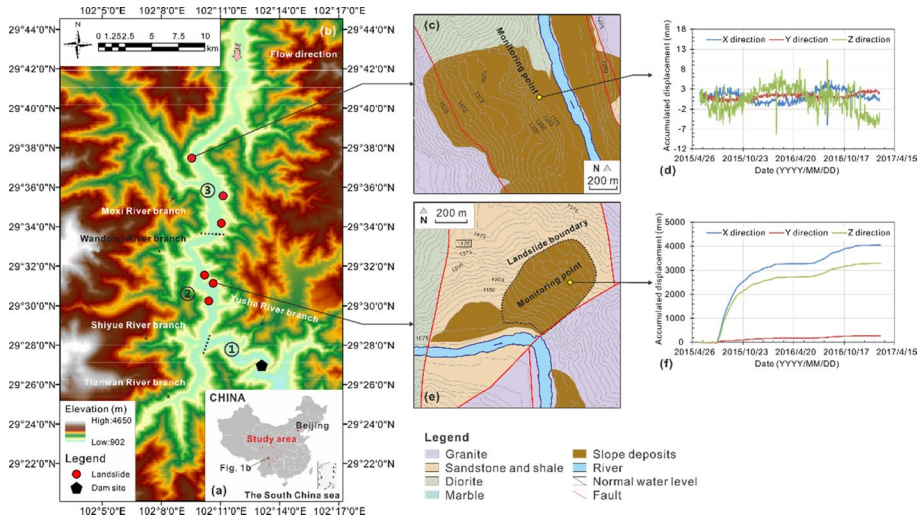
Fig. 2 Examples of slope deformation monitoring under the same hydrodynamic external load: **a** location; **b** topographic features with distribution of monitored slopes; **c** geology of Mogangling slope; **d** monitoring results of Mogangling slope; **e** geology of Xinhua slope; and **d** monitoring results of Xinhua slope

slope deposits usually occurs when the water level drops. When the water level returns to the normal water level, the deformation rate caused by the water-level drawdown gradually becomes smaller and the accumulated displacement tends to be constant. From the analysis of these monitoring results a new understanding of slope failure mechanisms can be developed: (1) For a slope, the action of external loading can make the landslide mass on the potential sliding surface produce a very small displacement, and the level of slope stability determines the mechanism by which the small displacement evolves into a large deformation; (2) for a slope with potential landslides, transient loads cause local displacement of the slope, but the stability of the slope is improved with the accumulation of displacement.

For this reason, Kou (1988) firstly proposed the radial slices method (RSM) and applied it to LEM. Then, Yi et al. (2017) combined the RSM with the energy method to propose a new evaluation method. Based on the previous work, this paper gives improvements in the method formulation to apply to a wide range of slope morphologies and gives more sufficient validation by parameter sensitivity and determination of the critical sliding surface than Yi et al. (2017). Secondly, we consider adequately a frame extension under hydrodynamic action. Finally, we apply the proposed method to the 1963 Vajont landslide and the Xinhua landslide to show its superiority.

2 General framework

2.1 Definition for the FOS

For a slope with landslide potential, the landslide mass has gravitational potential energy E_p. Based on the principle of energy conservation, when the landslide mass moves along the sliding surface, the gravitational potential energy will be reduced by ΔE_p and converted

to internal energy ΔU by overcoming the work of friction without accounting for other energy conversions, as shown in Eq. (1) (Yi et al. 2017).

$$\Delta E_p = \Delta U + \Delta E_k \tag{1}$$

Based on the above description, the stability of the slope can be evaluated as follows. The premise is that the landslide mass produces a small displacement ds along the sliding surface under external loading or self-weight action, and it belongs to the virtual displacement. Then, the FOS of the slope can be defined by the following equation (Yi et al. 2017):

$$\text{FOS} = \frac{\Delta U}{\Delta E_p} \tag{2}$$

According to Eq. (2), the stability of a slope can be determined by the ratio of the change in gravitational potential energy and the internal energy consumption after a small displacement has been generated. This relationship means that if $\Delta E_p < \Delta U$, then the FOS > 1, and the slope is in a stable state; if $\Delta E_p = \Delta U$, then the FOS = 1, and the slope is in a critically stable state; and if $\Delta E_p > \Delta U$, then the FOS < 1, and the slope is in an unstable state. This implies that the kinematic mechanism considered by the proposed framework is the generation of a small disturbance (small enough to be approximated as a slope in a stable state) under external load or self-weight action, which can convert into a large deformation (instability). This conversion process depends on the stability of the slope.

2.2 RSM

Before the stability analysis, the landslide mass must be divided radially. As shown in Fig. 3, the radial slices method decomposes the landslide mass by drawing a series of rays from the center of the sliding surface and dividing it into n 2D slices by equating the angle between the start and end of the landslide surface and the center of the sliding surface. This method therefore assumes that the sliding surface is circular or subcircular in shape. Commonly fitted shapes of sliding surfaces are a (1) circular arc; (2) elliptical arc; and (3) logarithmic spiral (the polar equation is $\rho = ae^{k(\theta - \theta_0)}$, where k, a and θ_0 are constants). Here, the sliding surface is assumed to be a circular surface, as an example. If enough slices are divided, the arc length at the base of each slice on the sliding surface can be approximated as the distance between the start and end points at the base of the slice, denoted by l_i. As

Fig. 3 Conceptual model of RSM. Keys: A is the left vertex of the slope; B_i and l_i are the left end point and the length of the bottom of the ith slice, respectively; C, O, and R are the right intersection with the landslide surface, the circle center, and the radius of the sliding surface; and γ and α are the angle of the line OB_1 with the line OA and the line OC, respectively
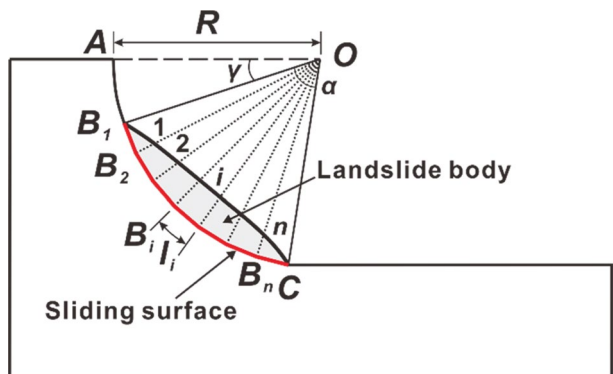
the slices are divided here by equal angles, the length of the sliding surface at the base of each slice is the same and is therefore denoted together by l.

2.3 Module of stability calculation

2.3.1 Change in gravitational potential energy

The slices of a landslide are numbered sequentially from top to bottom. The weight of the ith slice is denoted by W_i ($i = 1, 2, 3\ldots, n$), and the center of gravity is denoted by O_i. As the landslide mass produces a displacement ds along the sliding surface, the displacement of the center of gravity O_i of the ith slice is ds_i, and the displacement component in the vertical direction is ds_{yi}, as shown in Fig. 4. Then, the change in gravitational potential energy ΔE_p can be calculated using Eq. (3).

$$\Delta E_p = W_1 \mathrm{d}s_{y1} + W_2 \mathrm{d}s_{y2} + \ldots + W_i \mathrm{d}s_{yi} + \ldots + W_n \mathrm{d}s_{yn} = \sum_{i=1}^{n} W_i \mathrm{d}s_{yi} \tag{3}$$

The vertical displacement component is easier to calculate with an illustration, as shown in Fig. 4b. The change in gravitational potential energy of each slice is solved through the

Fig. 4 Calculation of the change in gravitational potential energy: **a** schematic diagram and **b** calculation of the geometric decomposition. Keys: ds is the preset virtual displacement; G_i and G_i' are the center of gravity of the ith slice before and after the motion, respectively; C and C' are the location of the bottom point of the landslide body before and after the motion, respectively; D_i is the auxiliary point; and other variables are defined in Fig. 3
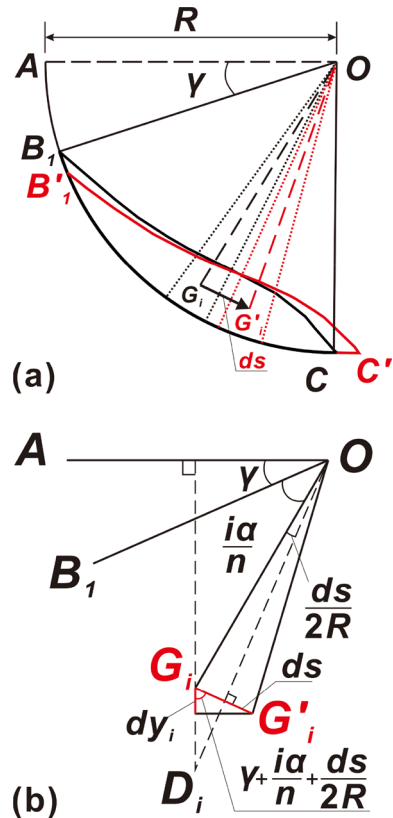
change in position of the slice's center of gravity. The distance from the center of gravity of the ith slice to the center of the circular sliding surface is denoted by r_i. If the landslide mass produces a displacement ds along the sliding surface, the displacement produced by the center of gravity of the ith slice can be calculated as $\overline{G_i G_i'} = 2r_i \sin(ds/2R)$.

Then, the vertical displacement component of the center of gravity of the ith slice can be obtained through Eq. (4).

$$ds_{yi} = 2r_i \sin \frac{ds}{2R} \cos \left(\gamma + \frac{i\alpha}{n} + \frac{ds}{2R} \right) \tag{4}$$

Substituting into Eq. (3) gives:

$$\Delta E_p = A_1 \sin \frac{ds}{R} + A_2 \cos \frac{ds}{R} - A_2 \tag{5}$$

where $A_1 = \sum\limits_{i=1}^{n} W_i r_i \cos(\gamma + i\alpha/n)$, and $A_2 = \sum\limits_{i=1}^{n} W_i r_i \sin(\gamma + i\alpha/n)$.

2.3.2 Internal energy consumption

The shearing of the base of each slice along the sliding surface is described by a Mohr–Coulomb strength criterion ($\tau = c + \sigma \tan \varphi$) and interpreted as the angle of internal friction φ versus the cohesive force c. If it is supposed that the direction of the force between the slices is parallel to the tangential direction of the sliding surface, that is, no work is performed to consume internal energy. Both Vardoulakis (2002) and Alonso et al. (2016) pointed out that the landslide mass generates heat by friction during shear motion, but in the concept of the proposed framework, the heat generated by this small disturbance is almost negligible. Then, only the work done by friction and cohesion along the sliding surface is considered in the proposed framework, and their calculation process is described separately.

The work done by friction is calculated using the following equation.

$$\Delta U_f = f ds = \mu W \cos \theta ds \tag{6}$$

where ΔU_f is the internal energy consumed to overcome friction, f is the sliding friction force, and μ is the coefficient of friction, obtained from $\mu = \tan \varphi$.

The work done by the cohesive force is calculated using the following equation.

$$\Delta U_c = cl ds \tag{7}$$

where ΔU_c is the internal energy consumed to overcome the cohesive force.

As shown in Fig. 5a, the black presentation indicates the pre-sliding state, and the red presentation indicates the post-sliding state. If the displacement of the sliding body along the sliding surface is ds, the angle of lines from the center of gravity of the ith slice of the pre-sliding state and post-sliding state to the center of the circular sliding surface is ds/R. Again, an illustration is needed here, as shown in Fig. 5b. Because the displacement of the sliding body along the sliding surface is very small, it can be approximated as a linear motion. By extending lines OA, OB_1 and OB_i to intersect the vertical line of the sliding surface at point OB_i' at A-, B_1- and B_i-, the angle between line $\overline{B_i B_i'}$ and the vertical direction yields $\theta_i = \gamma + (i-1)\alpha/R + ds/R$.

Fig. 5 Calculation of the internal energy consumption: **a** schematic diagram and **b** calculation of the geometric decomposition. Keys: B_i and B_i' are the left end point of the bottom of the ith slice before and after the motion, respectively; A-, B_1-, and B_i- are auxiliary points; and other variables are defined in Fig. 3
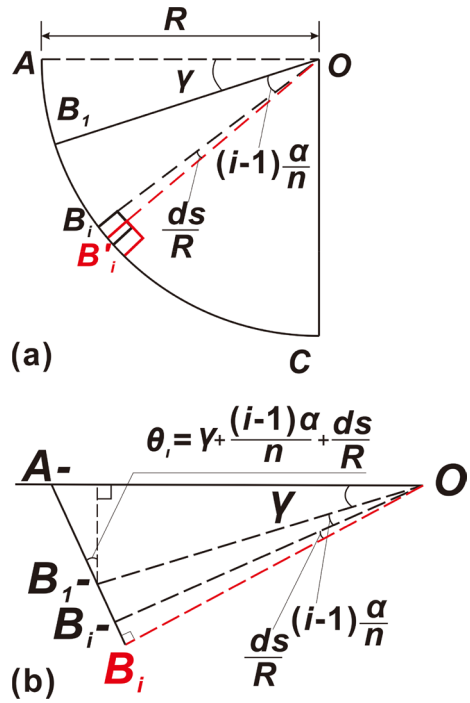
The internal energy consumed by the work done by the ith slice to overcome friction is shown as follows.

$$\Delta U_i = \Delta U_{fi} + \Delta U_{ci} = f_i ds + c\Delta s ds = W_i \mu \sin\left(\gamma + \frac{(i-1)\alpha}{R} + \frac{ds}{R}\right) ds + clds \quad (8)$$

Then, the work done by the landslide mass to overcome friction after it has produced a displacement ds along the sliding surface can be calculated as follows.

$$\Delta U = \sum_{i=1}^{n} \Delta U_i = \mu ds\left(A_3 \sin\frac{ds}{R} + A_4 \cos\frac{ds}{R}\right) + nclds \quad (9)$$

where $A_3 = \sum_{i=1}^{n} W_i \cos\left[\gamma + (i-1)\alpha/n\right]$, and $A_4 = \sum_{i=1}^{n} W_i \sin\left[\gamma + (i-1)\alpha/n\right]$.

2.3.3 Calculation of FOS

The gravitational potential energy change and the internal energy consumption can be calculated according to Eq. (5) and Eq. (9), respectively, and can be substituted into Eq. (2) to calculate the FOS of the slope, as follows.

$$\text{FOS} = \frac{\mu ds\left(A_3 \sin\frac{ds}{R} + A_4 \cos\frac{ds}{R}\right) + nclds}{A_1 \sin\frac{ds}{R} + A_2 \cos\frac{ds}{R} - A_2} \quad (10)$$

2.4 Module of instability dynamics analysis

In this conceptual model, as shown in Eqs. (1) and (2), external conditions resulting in a safety factor of less than 1 indicate that the change in gravitational potential energy is greater than the internal energy consumption. Then, the excess of the gravitational potential energy change will be converted into kinetic energy, and the landslide mass will be activated. During the movement, the landslide mass will dissipate internal energy due to the work done to overcome friction and cohesion. Therefore, the landslide mass always moves from a high energy state to a low energy state, and its gravitational potential energy, internal energy and kinetic energy are interconverted. The framework can be extended to allow the analysis of the energy state and the kinetic properties of a landslide during its movement. Except for the similar LEM that considers the landslide mass as a rigid mass for overall motion, this method considers the lateral side of each slice to remain perpendicular to the tangent direction of the intersection point of the sliding surface during the movement of the landslide mass from the arc surface to the flat surface, as shown in Fig. 6a.

Fig. 6 Calculation of landslide dynamics: **a** diagram before and after a certain distance of landslide movement; **b** geometric decomposition of gravitational potential energy change and **c** geometric decomposition of internal energy consumption. Keys: G_i' is the center of gravity of the ith slice when it is on a circular sliding surface; G_i'' is the center of gravity of the ith slice when it is on a flat sliding surface; and other variables are as shown above the figures
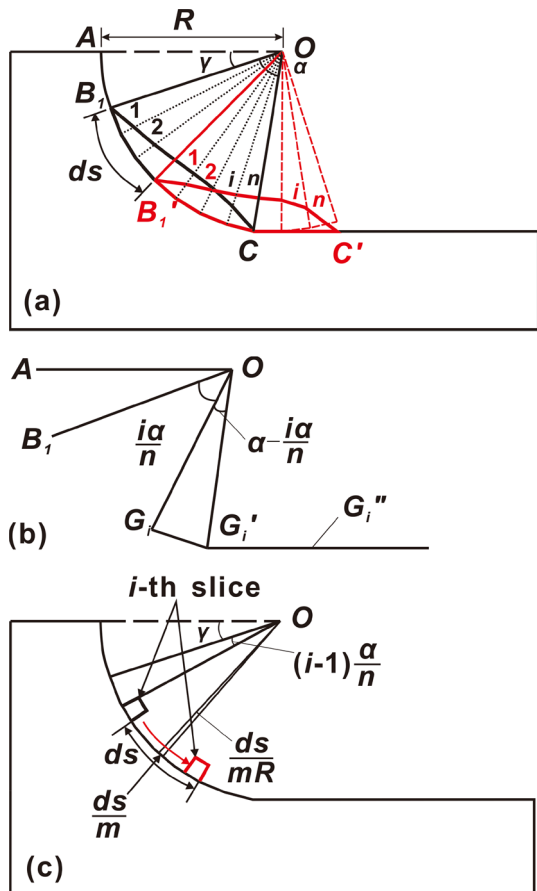
2.4.1 Change in gravitational potential energy

The motion of the ith slice is divided into two stages: on an arc surface and on a flat surface, and the change in the position of the center of gravity is resolved, as shown in Fig. 6b. The center of gravity changes from the initial point G_i to point G_i' when sliding on an arc surface and from point G_i' to point G_i'' when sliding on a flat surface. As known from Eq. (4), the ith slice generates a vertical displacement of $2r_i \sin\left[(n-i)\alpha/2n\right] \cos\left[\gamma + i\alpha/n + (n-i)\alpha/2n\right]$ after it moves from point G_i to point G_i', and the collated expression is given as $2r_i \sin\left[(n-1)\alpha/2n\right] \cos\left[\gamma + (n+i)\alpha/2n\right]$. When the slice moved onto a flat surface, the center of gravity changed from point G_i' to point G_i'' with a vertical displacement of the center of gravity expressed by $[ds - (n-i)l]\sin\beta + D_i[\sin(\gamma+\alpha) - \cos\beta]/2$. In the above expression, D_i is the average thickness in the radial direction, and β is the angle between the flat sliding surface and vertical direction.

To sum up, the vertical displacement of the center of gravity of the landslide when it undergoes movement with a displacement of ds can be obtained.

$$\overline{dS}_{yi} = 2r_i \sin\frac{(n-i)\alpha}{2n} \cos\left[\gamma + \frac{(n+i)\alpha}{2n}\right] + [ds - (n-i)l]\sin\beta + \frac{D_i}{2}\sin\left[(\gamma+\alpha) - \cos\beta\right] \tag{11}$$

When the slice moves from an arc surface to a flat surface, the law of change of the center of gravity of the block is inconsistent in the two stages. Then, the change in gravitational potential energy can be calculated in segments according to the relationship between different sliding displacements and the base of the bottom of the slices at different times as follows.

$$\Delta E_p = A_5 \sin\frac{ds}{R} + A_6 \cos\frac{ds}{R} - A_6 + A_7 ds + A_8, (k-1)l \le ds < kl, k = 1, 2, \ldots, n \tag{12}$$

where $A_5 = \sum\limits_{i=1}^{n-k+1} W_i r_i \cos(\gamma + i\alpha/n); A_6 = \sum\limits_{i=1}^{n-k+1} W_i r_i \sin(\gamma + i\alpha/n); A_7 = \sum\limits_{i=n-k+2}^{n} G_i \sin\beta;$

$$A_8 = \sum_{i=n-k+2}^{n} W_i\left\{2r_i \sin\left[(n-i)\alpha/2n\right] \cos\left[\gamma + (n+i)\alpha/2n\right]\right.$$

and
$$\left. -(n-i)\Delta s \sin\beta + h_i[\sin(\gamma+\alpha) - \cos\beta]/2\right\}.$$

2.4.2 Change in kinetic energy

The sum of the total kinetic energy change of the individual bars of the landslide, ΔE_k, is calculated as follows.

$$\Delta E_k = \frac{1}{2}\sum_{i=1}^{n} m_i v_i^2 = A_9 v_i^2 \tag{13}$$

where $A_9 = \sum\limits_{i=1}^{n} m_i(r_i/R)^2/2$.

2.4.3 Internal energy consumption

In the arc sliding surface section, the mode of work done by the frictional force of a slice is that of a variable force doing work on a curved trajectory, calculated using the infinitesimal method. As shown in Fig. 6c, the displacement ds is divided into m equal parts (where the magnitude of m tends to infinity), and the arc sliding surface length of each slice is ds/m. Assuming that the angle of slope within each part is constant and viewing the sliding surface as nearly straight, the movement of the slices is characterized by a constant force doing work in each small, equal part, with the central angle d$s/(mR)$ in each small, equal part.

The central angle at the jth equation of the 1st slice is $\gamma + jds/(mR)$; then, the work done by the frictional force on the jth equation of the 1st slice is shown as follows.

$$\Delta E_{f11j} = \left[W_1 \mu \sin\left(\gamma + \frac{jds}{mR} \right) + cl \right] \frac{ds}{m}, j = 1, 2, 3, \ldots, m \tag{14}$$

Next, the work done by the frictional force on the 1st slice over a displacement of ds is found to be as follows.

$$\Delta jE_{f11} = W_1 \mu \lim_{j \to \infty} \sin\left(\gamma + \frac{jds}{mR} \right) \frac{ds}{m} + clds \tag{15}$$

Integrating Eq. (15), the following equation is obtained.

$$\Delta E_{f11} = W_1 \mu R \left[\cos\gamma - \cos\left(\gamma + \frac{ds}{R} \right) \right] + clds \tag{16}$$

The formula for calculating the ith slice is obtained by mathematical induction.

$$\Delta E_{f1i} = W_i \mu R \left\{ \cos\left[\gamma + \frac{(i-1)\alpha}{n} \right] - \cos\left[\gamma + \frac{(i-1)\alpha}{n} + \frac{ds}{R} \right] \right\} + clds, i = 1, 2, 3, \ldots, n \tag{17}$$

The internal energy consumed to overcome the work of friction on the arc sliding surface when the 1st slice undergoes displacement ds is ΔE_{f1}, calculated as follows.

$$\Delta E_{f1} = \sum_{i=1}^{n} \Delta E_{f1i} = \mu R \left[A_{10} - A_{10} \cos\frac{ds}{R} + A_{11} \sin\frac{ds}{R} \right] + A_{12}ds, (k-1)l \leq ds < kl, k = 1, 2, 3, \ldots, n \tag{18}$$

where $A_{10} = \sum_{i=1}^{n-k+1} W_i \cos\left[\gamma + (i-1)\alpha/n \right]$, $A_{11} = \sum_{i=1}^{n-k+1} W_i \sin\left[\gamma + (i-1)\alpha/n \right]$, and $A_{12} = ncl$.

The internal energy consumed to overcome the work of friction on the flat sliding surface when the ith slice undergoes displacement ds is ΔE_{f2}, calculated using the following formula:

$$\Delta E_{f2} = A_{13} \frac{ds}{R}, (k-1)l \leq ds < kl, k = 1, 2, 3, \ldots, n \tag{19}$$

where $A_{13} = \sum_{i=n-k+2}^{n} W_i \cos\beta$.

2.4.4 Equations of motion

By bringing in Eqs. (12), (13), (18) and (19) to Eq. (1), the movement characteristics of the landslide mass after the slope instability can be calculated. The distance of the landslide mass movement is denoted by y, the velocity of movement by v and the acceleration of movement by a.

If $(k-1)l \leq y < kl(k = 1,2,\ldots,n)$, then the specific motion equation is shown as follows.

$$
\sqrt{A_5^2 + A_6^2} \cdot \sin\left(\frac{y}{R} + \psi_1\right) - A_6 + A_7 y + A_8 = A_9 v^2
$$
$$
+ \mu R\left[A_{10} + \sqrt{A_{10}^2 + A_{11}^2} \cdot \sin\left(\frac{y}{R} + \psi_2\right) + \frac{A_{12} y}{R}\right] + A_{13} y
$$

(20)

The final equation of motion is obtained by differentiating Eq. (20) by y.

$$
\frac{\sqrt{A_5^2 + A_6^2}}{R} \cdot \cos\left(\frac{y}{R} + \psi_1\right) + A_7 = 2A_9 a + \mu\sqrt{A_{10}^2 + A_{11}^2} \cdot \cos\left(\frac{y}{R} + \psi_2\right) + \mu A_{12} + A_{13}
$$

(21)

where $\tan\psi_1 = A_6/A_5$ and $\tan\psi_2 = -A_{10}/A_{11}$.

If $y > nl$, then the final motion equation is shown as follows.

$$
A_{14} = 2A_9 a + \mu A_{15} + A_{13}
$$

(22)

where $A_{14} = \sum_{i=1}^{n} G_i \sin\beta$ and $A_{15} = \sum_{i=1}^{n} G_i \cos\beta$.

3 Validation

The GEOSTUDIO commercial code is a mature and widely used tool for slope stability calculation based on the LEM and is well accepted in the technical and applied communities (GeoSlope International Ltd., 2007). In this paper, the proposed framework is validated by calculating cases from parameter sensitivity and automatic search sliding surface and comparing with GEOSTUDIO. The entire calculation process is implemented via MATLAB software.
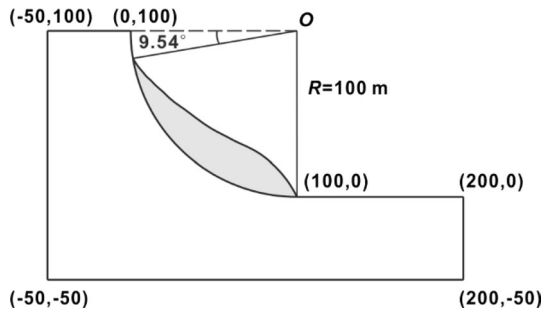

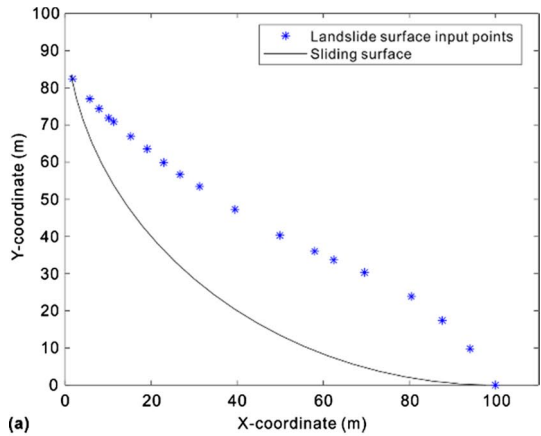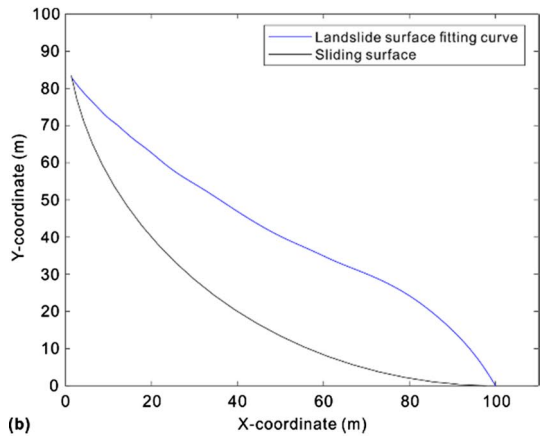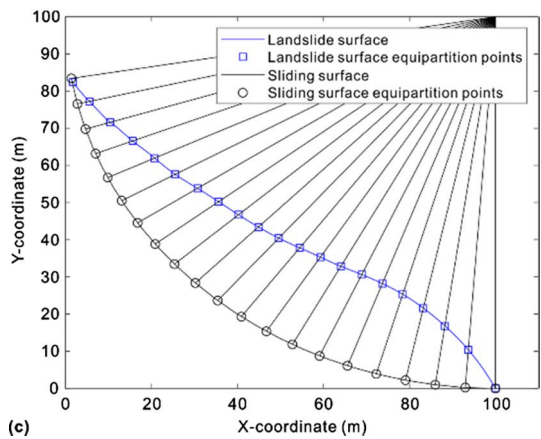**Fig. 7.** 2D geometric profile of Case 1

Fig. 8 Process of calculating the slope stability using the proposed method for Example 1: **a** input the coordinate points of the landslide surface; **b** fit the landslide surface; **c** radially strip the landslide mass; and **d** extract the information of the slices and calculate the FOS

Fig. 8 (continued)

(d)
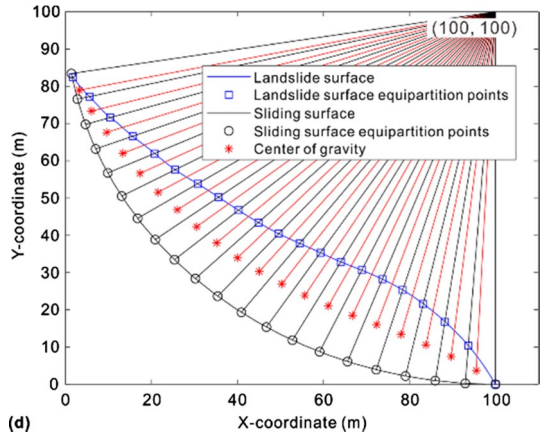
Table 1 Morphological characteristics of slices in the 2D profile using the RSM for Case 1

No	Area (m²)	X-coordinate of the center of gravity (m)	Y-coordinate of the center of gravity (m)	Distance from the center of gravity to the center of the circular sliding surface (m)
1	8.85	3.21	78.95	99.05
2	30.41	6.04	73.38	97.66
3	52.26	9.54	67.62	96.08
4	71.39	13.37	62.02	94.59
5	86.43	17.33	56.60	93.37
6	100.46	21.56	51.54	92.20
7	113.52	26.00	46.85	91.11
8	122.49	30.52	42.29	90.32
9	129.15	35.16	37.97	89.73
10	134.69	40.01	33.95	89.23
11	140.04	45.08	30.29	88.74
12	144.48	50.32	26.97	88.33
13	146.72	55.67	23.84	88.12
14	147.90	61.15	21.03	88.01
15	147.39	66.74	18.46	88.06
16	142.85	72.38	15.95	88.47
17	132.73	78.07	13.37	89.36
18	115.17	83.85	10.57	90.88
19	87.14	89.70	7.47	93.11
20	38.04	95.57	3.68	96.42

3.1 Parameter sensitivity

Case 1 is used for parameter sensitivity analysis. Figure 7 shows the geometric section of Case 1, and Fig. 8 demonstrates the process of using the proposed framework to calculate the FOS. The morphological characteristics of the slices obtained after using RSM to divide the landslide mass are shown in Table 1. There are three parameters for sensitivity
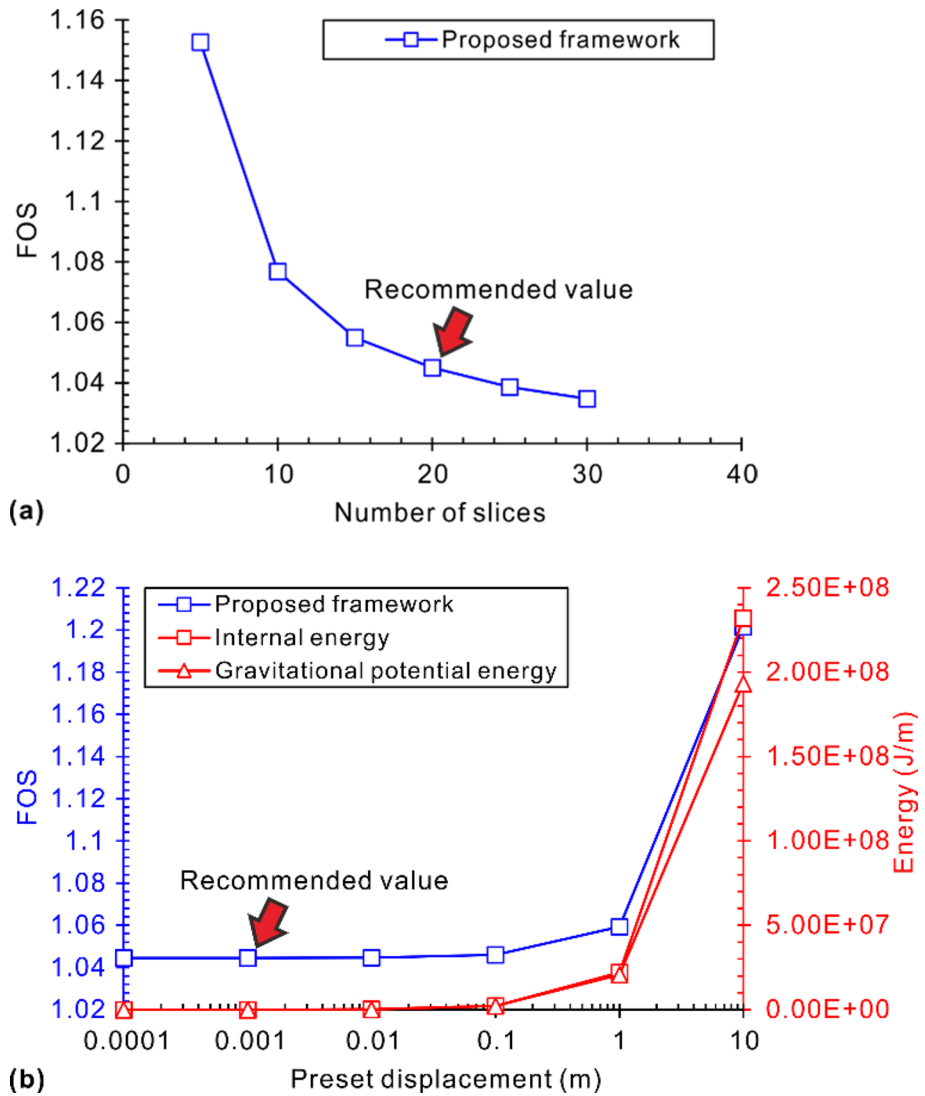
Fig. 9 Sensitivity analysis results of the proposed framework versus: **a** number of slices and **b** predetermined imaginary displacement

calculations here: (1) number of slices, (2) preset displacement and (3) shear strength. For the proposed framework, the number of slices and the preset virtual displacement affect the accuracy of the calculation results and not be compared with GEOSTUDIO. As shown in Fig. 9, as the number of slices increases or the virtual displacement decreases, the calculated value of the FOS gradually becomes smaller and converges. In order to ensure the calculation accuracy and reduce the calculation time as much as possible, the recommended number of slices for evaluating the stability of a slope is 20 and the preset displacement is 0.001 m. The calculated FOS in this case implies the possibility of a small disturbance in the slope under a specific load developing to a large deformation. If the stability of the
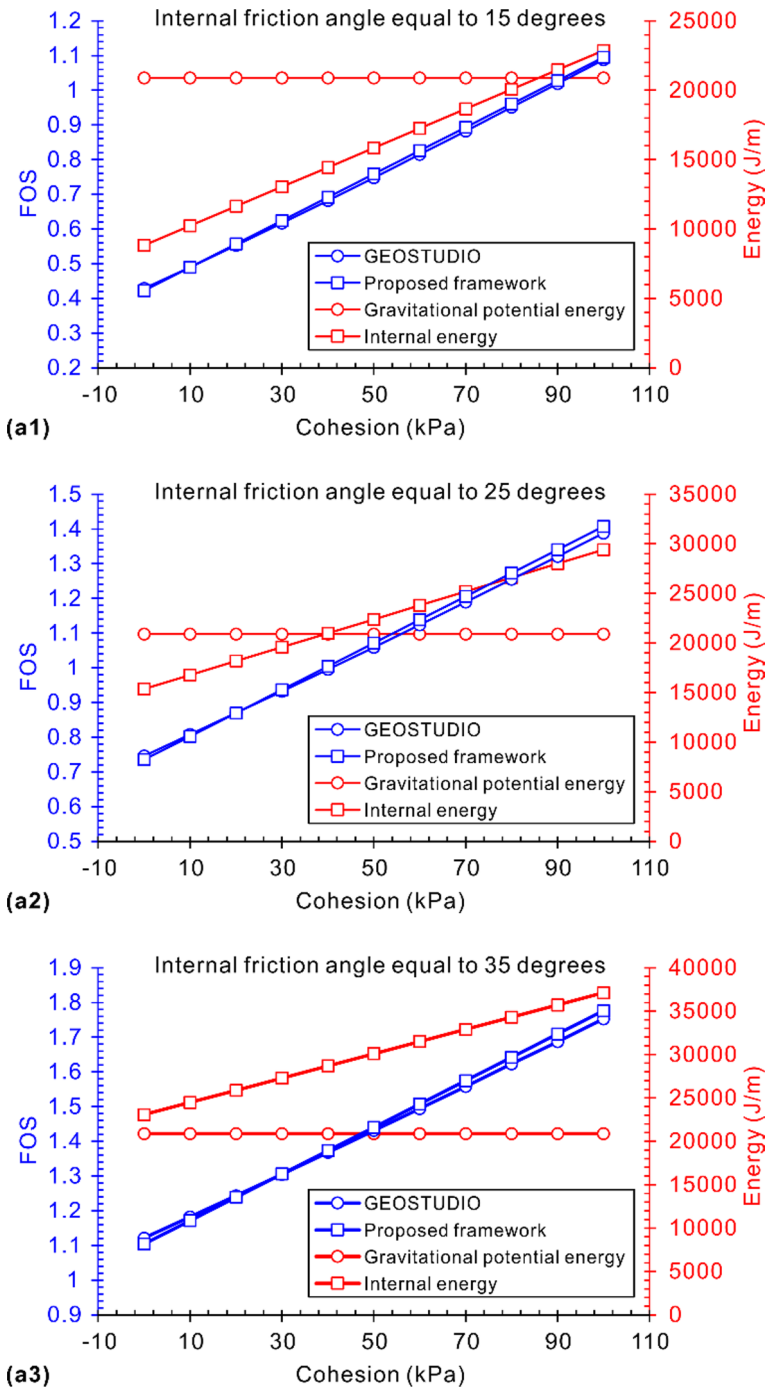
Fig. 10 Comparison between the sensitivity analysis results of the proposed framework and GEOSTUDIO: **a** cohesion and **b** internal friction angle
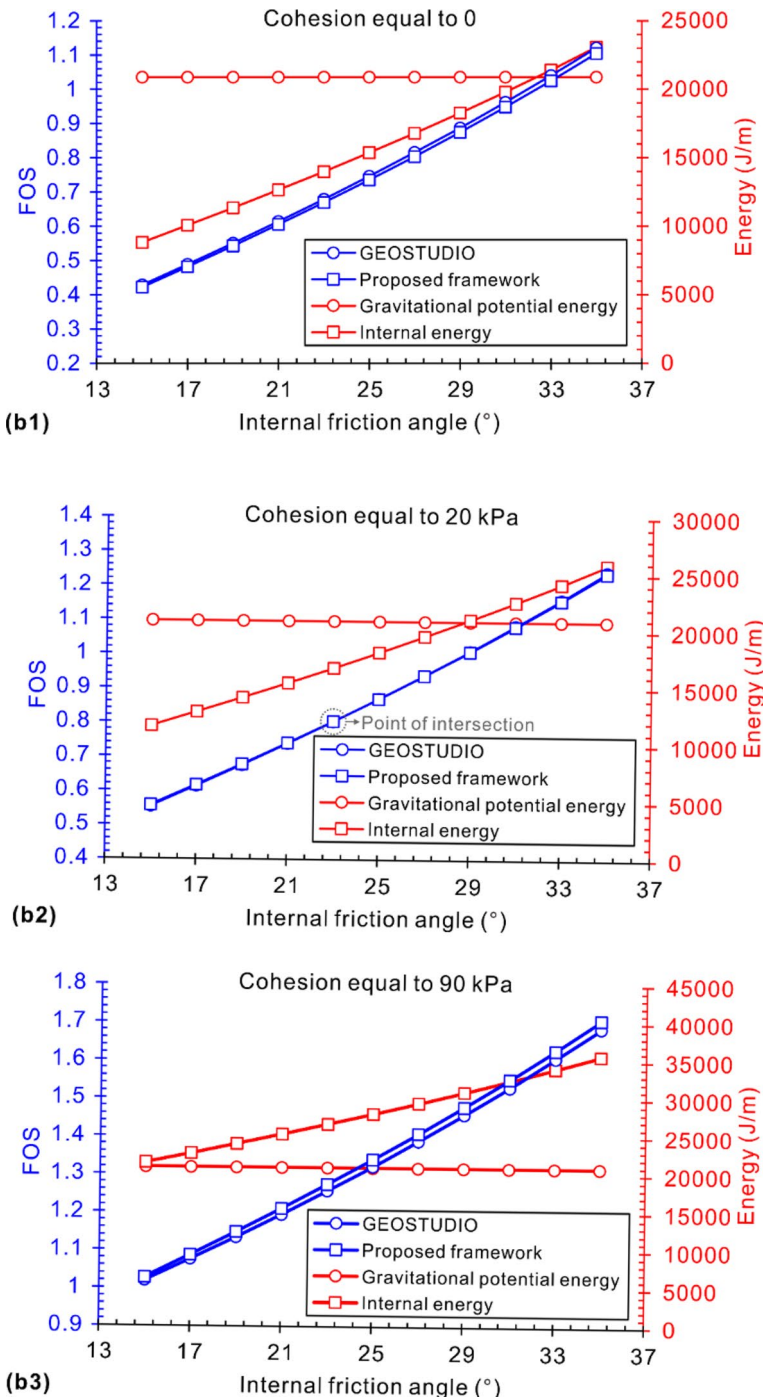
(b1)

(b2)

(b3)

Fig. 10 (continued)

slope after a certain displacement is generated is to be evaluated, the observed displacement value can be substituted for the previously set virtual displacement.

Shear strength (including cohesion and internal friction angle) is the determinant of slope stability and has been performed calculations by the proposed framework and GEOSTUDIO. The results of the sensitivity analysis of the shear strength are shown in Fig. 10, where the results of the two methods overlap very well and the sensitivity law remains consistent. Therefore, the results reflect the feasibility of the method proposed in this paper. Figure 10a shows the calculated FOSs of the Case 1 slope are for the general range of values of cohesion of geotechnical materials, for three different levels of internal friction angle, respectively. At the low cohesion level, the proposed framework analyzes the possibility of landslide on the slope is greater than that of the LEM. At high cohesion level, the conclusion is the opposite. There is a critical value of cohesion between the two phenomena that increases with the increase in the internal friction angle. Figure 10b shows the calculated FOSs of the Case 1 slope are for the general range of values of internal friction angle of geotechnical materials, for three different levels of cohesion, respectively. The results further validate the conclusions obtained in Fig. 10a. For the slope of Case 1, the cohesion is equal to 20kpa, and the FOSs calculated by the two methods are very close, and equal when the internal friction angle is equal to 23°.

3.2 Determination of the critical sliding surface

The determination of the critical sliding surface is another key issue in the analysis of slope stability. Determination of the critical sliding surface is essentially a process of repeated attempts to build a collection of possible sliding surfaces and calculate the corresponding FOS in turn, where the sliding surface with the lowest FOS is identified as the critical sliding surface. This trial procedure has several ways in define the shape of the sliding surface and to determine the location of the set of possible sliding surfaces. In the case where the sliding surface is considered to be circular, the commonly used methods are Grid and Radius method and Entry and Exit method. The innovation of the method to determine the critical sliding surface is not the focus of this paper, and this section is presented mainly to verify the feasibility of the method. Therefore, the combination of Grid and Radius method is chosen to combine the proposed framework and do the comparison calculation with GEOSTUDIO.
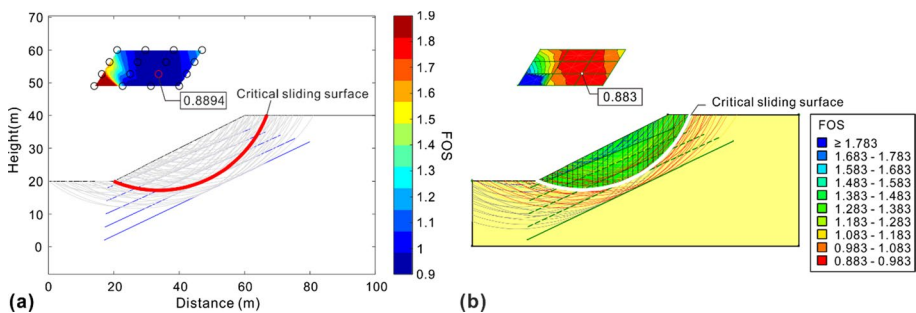

Fig. 11 Comparison between the determination results of critical sliding surface for Case 2: **a** the proposed framework and **b** GEOSTUDIO

Case 2 is derived from Yamin and Liang et al. (2010), which is presented mainly to show the refinement of the technical details of the presented framework. The slope of Case 1 is in only 1 quadrant on the coordinate axis distribution (Fig. 7), and the slope of Case 2 spans 2 quadrants (Fig. 11a). The tangent value of 90° is not present, giving trouble to the RSM, but is solved in the framework presented in this paper and is not described in detail. For the slope material of Case 2, cohesion, internal friction angle and unit weight are 20 kPa, 8° and 16 kN/m^3, respectively. Yamin and Liang et al. (2010) preset a sliding surface characterized by a circle center coordinate of (35.1, 55 m) and a radius of 38.12 m, and its FOS was calculated to be 0.95 by their method. In this section, the proposed framework and GEOSTUDIO are used to determine the critical sliding surface by the Grid and Radius method and calculate the minimum FOS for the Case 2 slope. As shown in Fig. 11, the critical sliding surface obtained by the two methods is identical and is characterized by a circle center with coordinates of (33.67, 52.67 m) and a radius of 35.44 m. The minimum FOS calculated by the proposed framework is 0.889, which is slightly larger than the 0.883 calculated by GEOSTUDIO. The feasibility of the proposed framework was verified from the sensitivity analysis of the shear strength and the comparison of the calculations in both aspects of determining the critical sliding surface.

4 Application to the reservoir landslide

The stability of reservoir slopes has been an enduring hot topic due to the special hydrological environment and the unpredictable catastrophic consequences once a landslide occurs. For example, the 1963 Vajont event is a tragic memory for the public because of the large economic and social losses. Compared to other landslide events, the data continue to be collected and the papers on the event continue to be published (Müller 1964, 1968; Selli and Trevisan 1964; Alonso and Pinyol 2010; Paronuzzi et al. 2013, 2016). Secondly in China, along with the commissioning of the Three Gorges Reservoir and the continuous development of hydropower in Southwest China, numerous cases of reservoir landslides or related research results have been reported (Zhou et al. 2017; Chen et al. 2018). As a typical case of a reservoir landslide, this paper uses the proposed framework for stability evaluation and destabilization dynamics analysis of the 1963 Vajont event. In analyzing the deformation patterns of the 1963 Vajont event, it is found that there are some landslides in the Chinese reservoir area with different deformation patterns. Therefore, when doing the slope stability evaluation, the slopes of the two deformation modes are calculated and compared, and the failure mechanism is summarized.

4.1 Stability analysis and failure mechanism

The 1963 Vajont landslide is characterized by limestone masses and belongs to rock landslide and reactivation of an ancient landslide. Alonso and Pinyol (2010) and Paronuzzi et al. (2013) described the characteristics and behavior of groundwater, specifically the high permeability of the slope material above the sliding surface, influenced by the continuous fracture of the rock mass and karstic phenomena. Therefore, in the filling-drawdown cycles of reservoir water level, the pore water pressure inside the slope can be dissipated in time, and the groundwater level can be approximated as always maintaining the same level with the reservoir water level. The Xinhua landslide is characterized by ancient landside deposits, and a preliminary study has presented previously by Chen et al. (2018). Chen
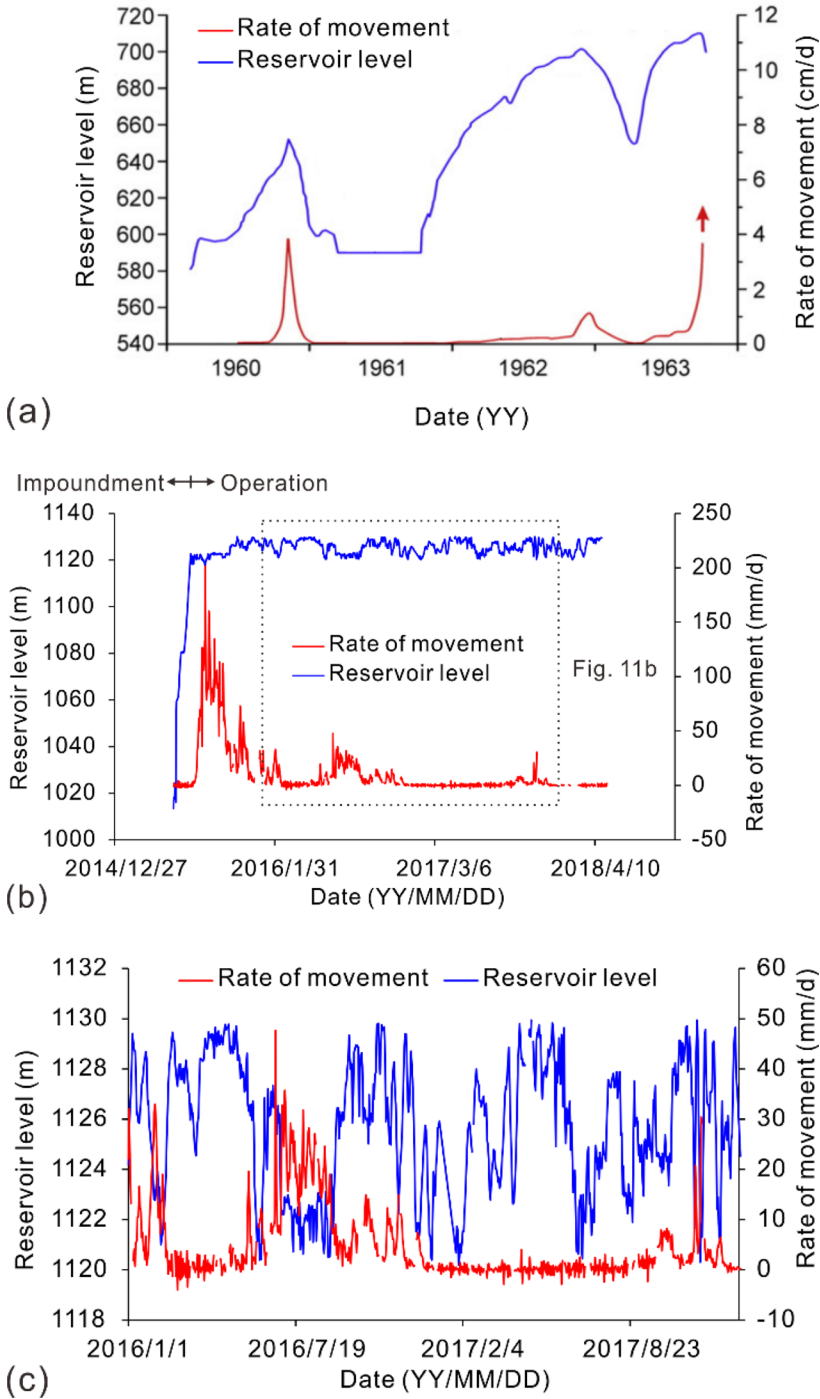
Fig. 12 Deformation performance of landslides and correlation with water-level changes: **a** the 1963 Vajont landslide (Paronuzzi et al. 2013); **b** since the start of impoundment for the Xinhua deposit landslide (Chen et al. 2018) and **c** in the operation period for the Xinhua deposit landslide (Chen et al. 2018)

et al. ([2018](#)) found that the slope deposits are low-permeability materials, and the pore water pressure inside the slope fails to dissipate in time when the reservoir water level has a drawdown during the rainy season, and the drawdown of the groundwater level lags behind the reservoir water level (Fig. 12). Zhang et al. ([2020](#)) found a similar phenomenon in the Majiagou landslide in the Three Gorges Reservoir area.

Usually, the slope stability with groundwater variations is analyzed by uncoupled analysis, and the hydraulic results obtained by the finite element method are imported into the stability analysis framework and calculated. In the absence of an effective means of importing the results of the finite element method to the proposed framework, reasonable assumptions regarding patterns of groundwater changes are feasible based on the monitoring results of landslides with different permeabilities referring to the approach of Alonso and Pinyol ([2010](#)) and Segui et al. ([2020](#)), as shown in Fig. 13. This assumption is mainly for the operation period, i.e., after a stable seepage field has been formed inside the slope for the normal water level, agreeing with change characteristics revealed by hydrological monitoring of slope feature points and the simulation of Tang et al. ([2019](#)).

When the water-level changes, the possible presence of internal pore water pressure, hydrostatic pressure on the toe of the slope, and seepage force due to water-level differences can lead to a new limit equilibrium. The changes in the mechanical behavior of individual slice are analyzed for the case of possible water-level changes inside the slope, as shown in Fig. 14. The shearing of the base of each slice along the sliding surface under fluctuation of water level is described by a combination of Mohr–Coulomb strength criterion and Terzaghi's effective stress principle ($\tau = c + \sigma' \tan \varphi = c + (\sigma - p) \tan \varphi$) (Lade and De Boer [1997](#); Jiang and Xie [2011](#)). When applied to the proposed framework, for the ith slice, take the midpoint P_i at the base of the slice and make an isopotential line intersecting the water-level line at P_i'. The vertical height H_{ci} of line $\overline{P_i P_i'}$ is considered the average pressure head on the base of the ith slice. Then, the equation for calculating the internal energy consumption becomes as shown below.

$$\Delta U_f = f \mathrm{d}s = \left[\mu \left(W \cos \theta - \gamma_w H_c l\right) + cl\right] \mathrm{d}s \tag{23}$$

where γ_w indicates the water capacity.

For low-permeability materials, there is a situation in which the equipotential line of flow is not vertical, and thus, it needs to be corrected for pore water pressure. The following equation is used for correction:

$$H_c = H_w \cos^2 \beta \tag{24}$$

where H_w is the vertical distance from the base center of the slice to the piezometric line; H_c is the pore pressure at the base center of the slice; and β is the angle between the piezometric line and the horizontal direction.

Bear ([1972](#)) explained that the seepage force can be calculated by

$$S = \gamma_w A_{\mathrm{sat}} \Delta H \tag{25}$$

where γ_w is the unit weight of water, A_{sat} is the area of the saturated zone, and ΔH is the difference in the water level within the side slope. In the proposed framework, the work done by seepage force is incorporated into internal energy consumption.

For the determination of strength parameters, for the 1963 Vajont landslide, Paronuzzi et al. ([2013](#)) suggested a cohesion of 0 kPa and a range of values for the internal friction angle in [17.5°, 27°], so in this calculation the cohesion was determined to be 0 kPa and
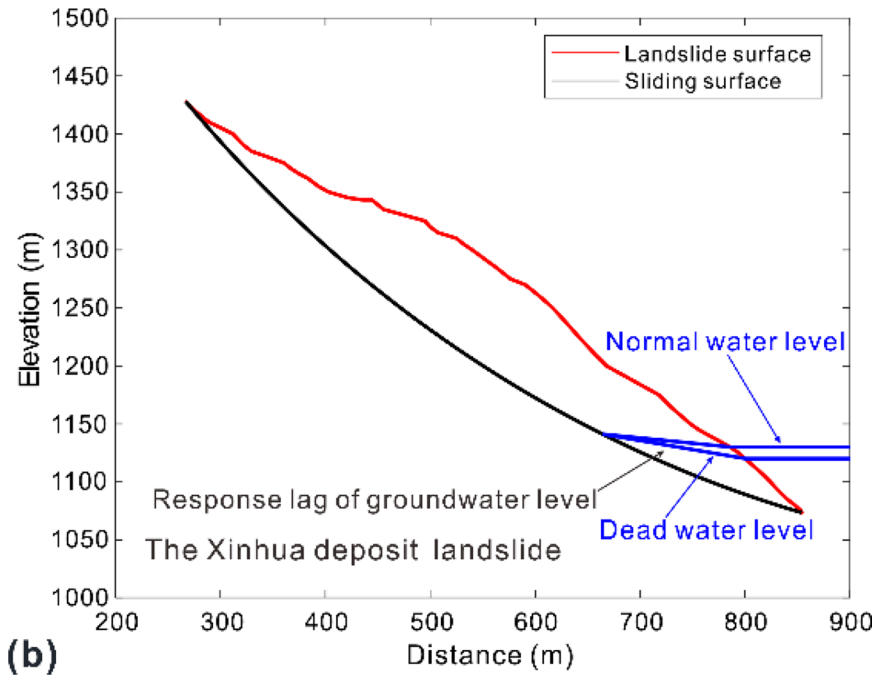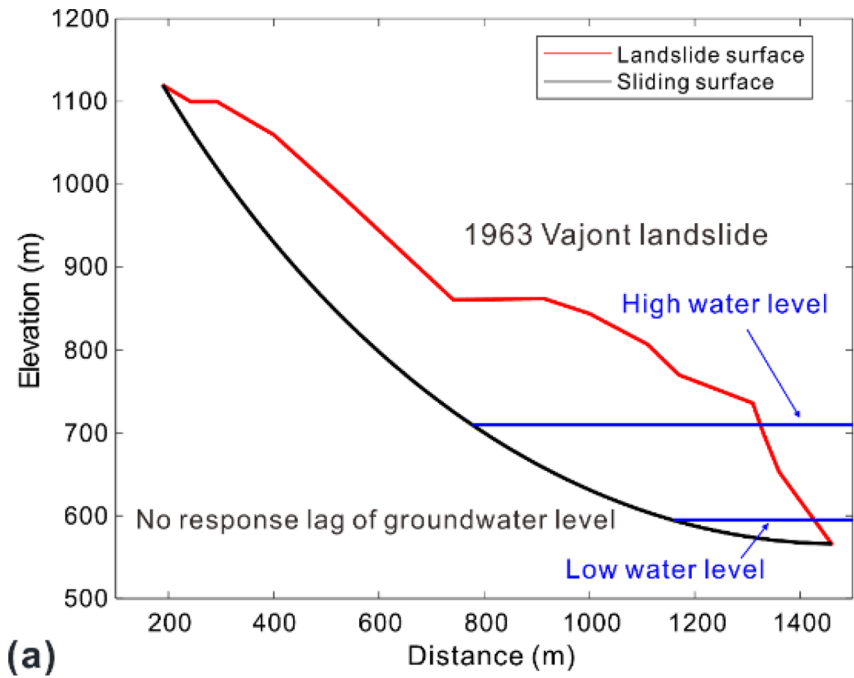
Fig. 13 Reasonable assumptions on the variation patterns of groundwater levels in landslides with different materials: **a** the 1963 Vajont landslide and **b** the Xinhua landslide in the Dagangshan reservoir

Fig. 14 Treatment of the slices in different water-level situations: **a** horizontal groundwater level, **b** groundwater level at an angle to the horizontal; and **c** the slice is inundated by reservoir water
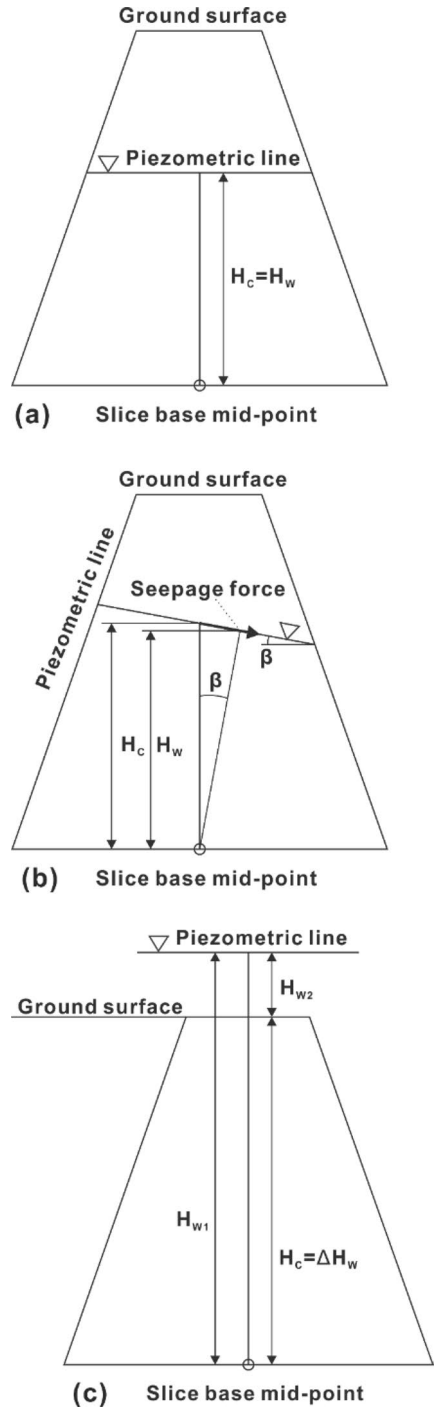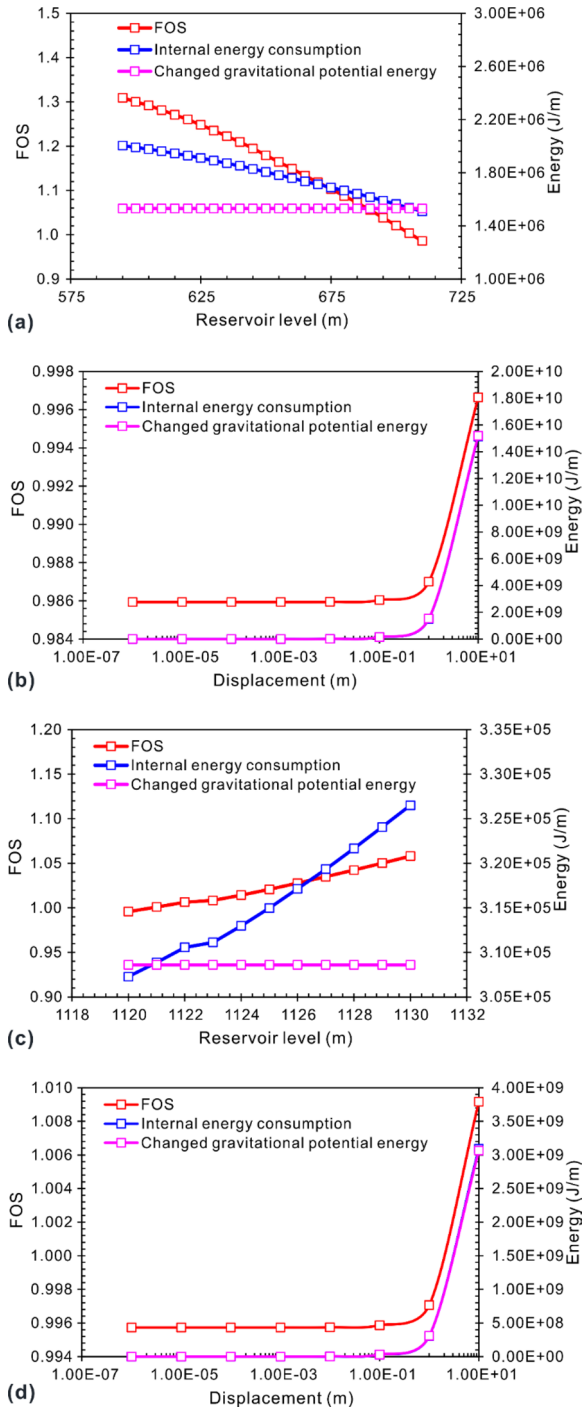
Fig. 15 Results of slope stability calculations: **a** correlation with the water level for the 1963 Vajont landslide, **b** correlation with the displacement for the 1963 Vajont landslide, **c** correlation with the water level for the Xinhua deposit landslide, and **d** correlation with the displacement for the Xinhua deposit landslide

the internal friction angle to be 26°. For the Xinhua deposit landslide, the cohesion is taken as 12 kPa and the internal friction angle is taken as 35.8° according to Chen et al. (2018; 2021). The location of the sliding surface was determined based on available geological data. As shown in Fig. 15, FOSs of two landslides can be obtained based on the water-related force conditions that precede the failure occurrence and the displacement of the landslide mass.

In terms of the influence by reservoir-level changes, the calculation result of 1963 Vajont landslide shows the reduction of the FOS with the rising of reservoir water level, which is consistent with the monitoring results, i.e., the response pattern of increasing deformation rate as the reservoir level rises. The high permeability of the slope material determines that the groundwater level can keep changing simultaneously with the reservoir water level. In this case, the rise in reservoir level leads to an increase in pore water pressure on the sliding surface, a decrease in effective stress as well as a decrease in shear resistance. Therefore, the pore pressure effect leads to a positive correlation between reservoir water level and deformation rate (Fig. 16a). The calculation of Xinhua landslide shows the decrease in the FOS with the decrease in reservoir water level and is in line with the accelerated deformation rate due to the drawdown of reservoir water level as shown by deformation monitoring. The low permeability of the slope materials results in a delayed response of the groundwater level as the reservoir level decreases. This is the result of the combined effect of the permeability properties of the material and the rate of reservoir-level change, so this delay only occurs when the water level is falling rapidly or when there is continuous heavy rainfall at the same time (Fig. 16b, c). The delayed response of the groundwater level leads to transient seepage within the slope and a seepage force in the same direction, which favors the shear forces on the sliding surface and therefore leads to a decrease in slope stability. In terms of the influence by deformation accumulation, for both landslides, the FOSs gradually increase with the accumulation of displacements. Reflected in the deformation monitoring data is that the rate of movement will gradually become smaller with the accumulation of displacement when the hydrodynamic load that causes the rate of movement disappears. This result verifies the cumulative deformation to failure mechanism of reservoir landslides; that is, the occurrence of landslides is not caused by one-phase deformation, but is the result of multi-phase deformation accumulation. External load per cycle occurrence causes a decrease in slope stability. However, the landslide is self-stabilized by cumulative deformation until it reaches the critical point of creep to high-speed motion. Therefore, it leads to the step-type characteristics of the displacement–time curve for reservoir landslide, as shown in Fig. 1c, d.

4.2 Instability dynamic analysis

Hendron and Patton (1987) stated that the 1963 Vajont landslide reaches a maximum velocity of 20–25 m/s during its movement. The normal value internal friction angle of clay is taken to be unable to support the transition from slow creep to fast movement, so strength degradation must have occurred during the movement. Therefore, the determination of the internal friction angle/friction coefficient and the strength degradation have been a major research focus of the 1963 Vajont event. Ciabatti (1964) gave a value of 0.236 for the coefficient of friction based on simple mechanical considerations. In addition, Ghirotti (1994) gave values for the internal friction angle of 8°–12° (corresponding to a friction coefficient of 0.14–0.21). Hendron and Patton (1985) reported direct shear tests on remolded specimens with measured residual friction angles of 8°–10° and concluded

Fig. 16 Failure mechanism of reservoir landslide during filling-drawdown cycles: **a** high-permeability landslide with the rising of reservoir water level, **b** low-permeability landslide by rapid drawdown of reservoir water level in the annual-regulation reservoir, and **c** by the combination drawdown of reservoir water level and continued heavy rainfall in the daily-regulation reservoir
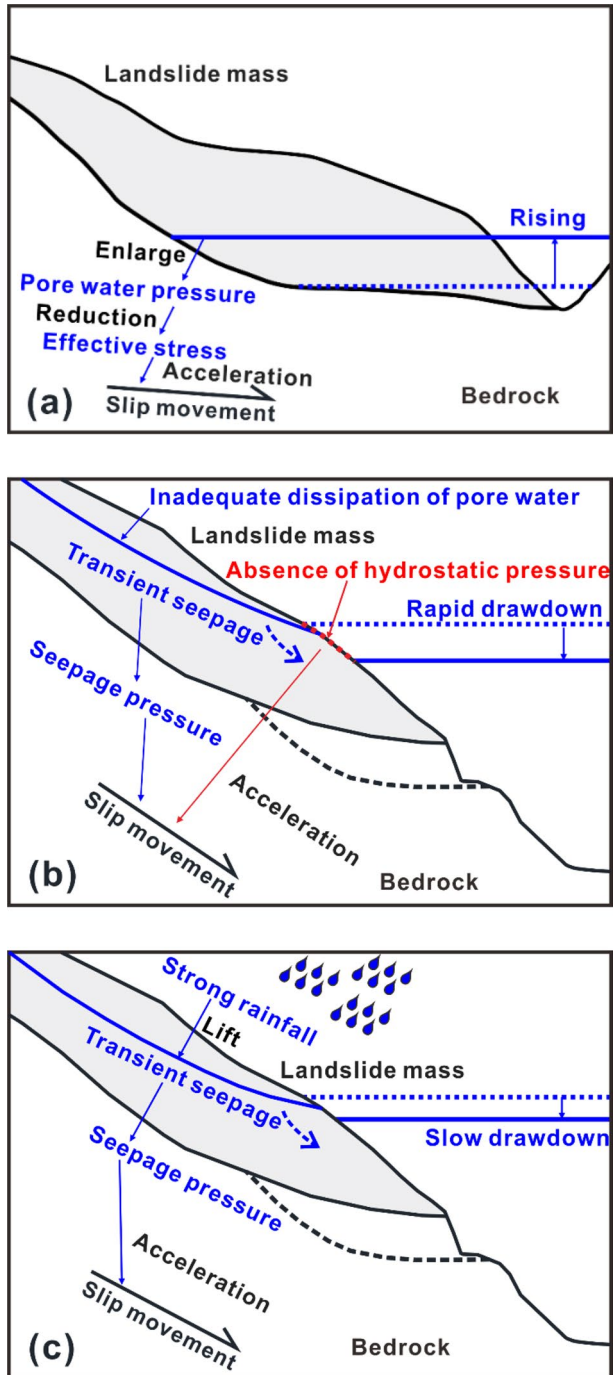
that the friction coefficient decreased by about 50% during the actual movement. Tika and Hutchinson (1999) used a ring shear to find the residual strength on remolded specimens and learned that when the relative shear displacement exceeded 200 mm, the residual friction angle was 10°; at a shear rate of 0.1 m/s, the residual friction angle decreased further and reached a lower value of 5°.

To reenact the movement process, Zaniboni and Tinti (2014) performed a sensitivity analysis based on the UBO-BLOCK1 code. The code UBO-BLOCK1 was developed and is currently maintained by a team of researchers at the University of Bologna and can be used to analyze landslide dynamics based on a one-dimensional numerical Lagrangian model. The numerical simulation is between friction coefficients of 0.08–0.46 and finally determined a constant friction coefficient of 0.20 to be used in the calculation. In this paper, the proposed framework is adopted with the friction coefficient setting equally constant and 0.2, and the calculated results are compared with Zaniboni and Tinti (2014). Zaniboni and Tinti (2014) presented calculation results for a total of six profiles, but the presentation of the geomorphology of profile 1 was not available for modeling, so only profiles 2–6 were selected for comparison as shown in Fig. 17.

Figure 18 shows the comparison between the proposed framework and the method of Zaniboni and Tinti (2014) for the calculation of the movement process of the 1963 Vajont landslide. In the middle section, the calculation results of the two methods have good agreement. However, since the proposed framework belongs to a 2D method, while the method of Zaniboni and Tinti (2014) belongs to a 3D method, the computational results of this paper have a large dispersion. This dispersion is acceptable if the morphology and slope angle of the sliding surface of the non-intermediate section are observed. The proposed framework calculates the average value of the maximum velocity as 28.59 m/s, and the maximum velocity of the middle section is 21.51 m/s, which is basically in accordance with the statement of Hendron and Patton (1987) for the maximum velocity of 20–25 m/s. In contrast, the calculation of Zaniboni and Tinti (2014) is conservative and the average value of the maximum velocity is less than 20 m/s.

5 Discussions

For the framework proposed in this paper, we have done some validation studies and functional extensions and applications to further discuss some meaningful issues as follows.

(1) The sensitivity analysis of strength ensures the accuracy of the proposed framework in the evaluation of slope stability. The proposed framework is implemented based on RSM and LEM is implemented based on VSM. The analysis results show that the landslide potential of the composite damage mode of rotation plus translation is greater than that of translation only at low cohesion levels; the landslide potential of the translation-only failure mode is greater than that of the composite mode at high cohesion levels. For the case 1 used in this paper, this boundary value to distinguish between high and low viscous cohesion levels is 23 kPa.

(2) The sensitivity analysis of the strength is based on a known sliding surface. In specific cases where there are in situ measurements with instruments such as inclinometers, the sliding surface is known, but there is usually uncertainty in the location of the sliding surface in more cases. Therefore, the validation is sufficient to illustrate the feasibility of the proposed framework while ensuring reliable results for determining the criti-

Fig. 17 Geological profiles of the 1963 Vajont landslide and the results of their division by RSM: **a** profile 2, **b** profile 3, **c** profile 4, **d** profile 5, and **e** profile 6
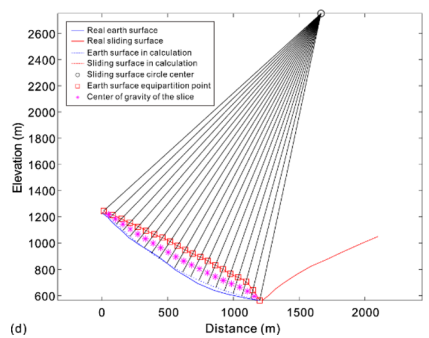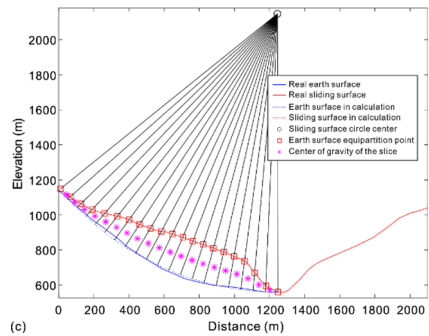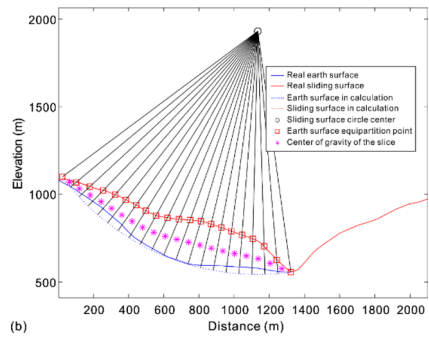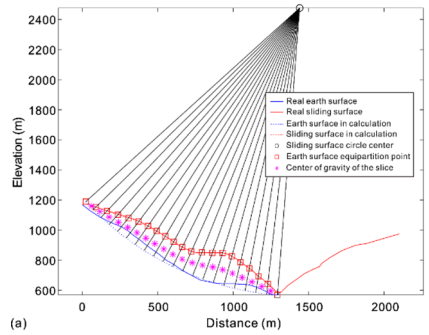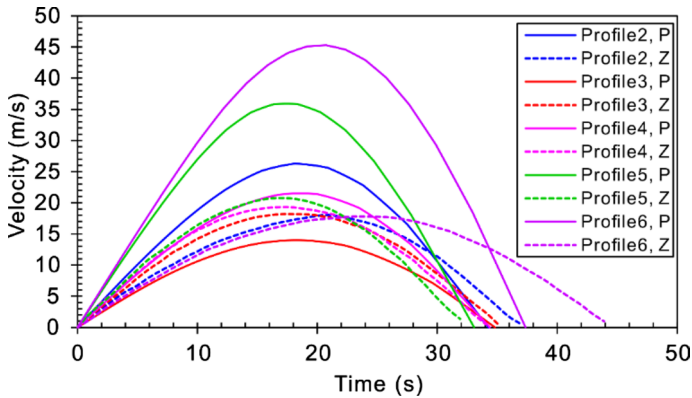
Fig. 18 Calculation results of instability dynamic analysis for 1963 Vajont landslide

cal sliding surface. From the calculation principle, the LEM, taking Janbu method as an example, it calculates slope stability from the relationship of forces, i.e., the ratio of shear resistance force to shear force. The proposed framework assumes of virtual displacement, which is solved from the perspective of energy change. The increment of internal energy consumption is solved by the shear resistance force along the sliding surface, and the increment of gravitational potential energy is solved by the shear force along the sliding surface. Therefore, the similarity in principle is the basis for the feasibility of this method. To a certain extent, the present method belongs to the extension of LEM, which in turn enables more functions including evaluation of slope stability on cumulative displacement and analysis of landslide dynamics after instability.

(3) The proposed framework can evaluate slope stability under water-level changes by considering the Terzaghi's effective stress principle, interpretation of seepage force by Bear (1972), and the correction of pore water pressure. The proposed framework is applied to the 1963 Vajont event and a deposit landslide with a different deformation pattern, in the absence of the importing means of the seepage analysis results (for example, through FEM) and reasonable assumptions of water-level change patterns referring to Alonso and Pinyol (2010) and Segui et al. (2020). This hypothesis can well explain the change of groundwater within the slope when the reservoir level changes, which is consistent with the characteristic point monitoring of the real slope and the simulation of Tang et al. (2019). Based on this, the stability analyses of two landslides at different water levels were carried out, and the results of the calculations conformed to the actual deformation pattern. In addition, the study of the effect of cumulative displacement well explains the step-type characteristics of the displacement–time curve for the reservoir landslide. However, how to go about identifying the critical point of creep to high-speed motion is the future work that needs to be done.

(4) By considering the strength degradation, the proposed framework can well simulate the motion process after the instability of 1963 Vajont landslide. Due to the limitations of the 2D method, the dispersion of the calculated results for different cross sections is large if the morphology of the sliding surface varies greatly at different locations. In this case, the calculation results of the intermediate section are representative. Based on the geological profile given by Zaniboni and Tinti (2014), the average value of the

maximum velocity during motion was calculated to be 28.59 m/s and the maximum velocity of the middle section is 21.51 m/s, in accordance with Hendron and Patton (1987).

6 Conclusions

A novel and robust slope stability evaluation method based on RSM and energy method is proposed in this paper. In the course of research and application, a number of advantages and features of this method were found compared to traditional and commonly used LEM: (1) this method considers the failure mode of the slope as a combination of translation and rotation, instead of the general belief of only translation along the sliding surface, which is more in line with the actual monitoring results; (2) if the virtual displacement is regarded as a variable, the effect of accumulated displacement on slope stability can be studied; and (3) if the FOS for the slope is less than 1, this method can be extended to analyze movement of landslide mass after instability using the energy balance. The proposed framework has a broader application prospect compared to LEM and has been applied to 1963 Vajont event and Xinhua event. The calculations show that permeability of slope materials is the key to understanding landslide hazards in reservoir areas. The 1963 Vajont landslide is characterized by highly permeable material, and the groundwater level can maintain the same height as the reservoir level when it changes. Therefore, the failure mechanism is the reduction of effective stress caused by the increased pore water pressure when the water level rises. The Xinhua deposits landslide is a low-permeability material. Its failure mechanism is seepage force by that the groundwater level fails to react in time to form a water-level difference when the reservoir water level drops rapidly or water-level drop occurs simultaneously with continuous heavy rainfall.

Declarations

Conflict of interest The authors declare that they have no known competing financial interests or personal relationships that could have appeared to influence the work reported in this paper.

References

Alonso EE, Pinyol NM (2010) Criteria for rapid sliding. I A review of Vaiont case. Eng Geol 114(3–4):198–210

Bandara S, Ferrari A, Laloui L (2016) Modelling landslides in unsaturated slopes subjected to rainfall infiltration using material point method. Int J Numer Anal Met 40(9):1358–1380

Bear J (1972) Dynamics of Fluids in Porous Media. American Elsevier Pub. Co

Carlà T, Intrieri E, Raspini F, Bardi F, Farina P, Ferretti A, Colombo D, Novali F, Casagli N (2019) Perspectives on the prediction of catastrophic slope failures from satellite InSAR. Sci Rep 9(1):14137

Chen ML, Lv PF, Zhang SL, Chen XZ, Zhou JW (2018) Time evolution and spatial accumulation of progressive failure for Xinhua slope in the Dagangshan reservoir, Southwest China. Landslides 15:565–580

Ciabatti M (1964) La dinamica della frana del Vajont. Museo geologico Giovanni Capellini XXXII:139–153 (in Italian)

Fan X, Xu Q, Liu J, Subramanian SS, He C, Zhu X, Zhou L (2019) Successful early warning and emergency response of a disastrous rockslide in Guizhou province, China. Landslides 16:2445–2457

Fredlund MD (2009) SVSlope User's manual. SoilVision System Ltd., Saskatoon, Canada

Fredlund DG, Krahn J (1977) Comparison of slope stability methods of analysis. Can Geotech J 14(3):429–439

Fredlund DG, Krahn J, Pufahl DE (1981) The relationship between limit equilibrium slope stability methods. Proc Int Conf Soil Mech Found Eng 3:409–416

GeoSlope International Ltd. Seep/W user's guide for finite element seepage analysis. Calgary, Alta: GEO-SLOPE International Ltd, 2007

Ghirotti M (1994) Modellazione numerica della frana del Vajont sulla base di nuovi dati. Geol Romana 30:207–216 (**in Italian**)

Girardi V, Ceccato F, Rohe A, Simonini P, Gabrieli F (2022) Failure of levees induced by toe uplift: Investigation of post-failure behavior using material point method. J Rock Mech Geotech

Guzzetti F, Peruccacci S, Rossi M, Stark CP (2007) Rainfall thresholds for the initiation of landslides in central and southern Europe. Meteorol Atmos Phys 98:239–267

Guzzetti F, Peruccacci S, Rossi M, Stark CP (2008) The rainfall intensity–duration control of shallow landslides and debris flows: an update. Landslides 5:3–17

Hendron AJ, Patton FD (1985) The Vaiont slide, a geotechnical analysis based on new geologic observations of the failure surface. Technical Report GL-85–5. Department of the Army, U.S. Army Corps of Engineers, Washington, DC

Hendron AJ, Patton FD (1987) The Vaiont slide - A geotechnical analysis based on new geologic observations of the failure surface. Eng Geol 24:475–491

Intrieri E, Raspini F, Fumagalli A, Lu P, Conte SD, Farina P, Allievi J, Ferretti A, Casagli N (2018) The Maoxian landslide as seen from space: detecting precursors of failure with Sentinel-1 data. Landslides 15:123–133

Jiang H, Xie Y (2011) A note on the Mohr-Coulomb and Drucker-Prager strength criteria. Mech Res Commun 38(4):309–314

Kou RM (1988) Radially cutting method-A new method to analyse the stability of soil slopes. Hydrogeol Eng Geol 03:47–50 (**in Chinese**)

Lade PV, De Boer R (1997) The concept of effective stress for soil, concrete and rock. Geotechnique 47(1):61–78

Li HB, Qi SC, Yang XG, Li XW, Zhou JW (2020) Geological survey and unstable rock block movement monitoring of a post-earthquake high rock slope using terrestrial laser scanning. Rock Mech Rock Eng 53(10):4523–4537

Lin S, Zheng H, Han B, Li Y, Han C, Li W (2022) Comparative performance of eight ensemble learning approaches for the development of models of slope stability prediction. Acta Geotech 17(4):1477–1502

Liu SY, Shao LT, Li HJ (2015) Slope stability analysis using the limit equilibrium method and two finite element methods. Comput Geotech 63:291–298

Lu N, Godt J (2008) Infinite slope stability under steady unsaturated seepage conditions. Water Resour Res 44(11)

Lu N, Likos WJ (2006) Suction stress characteristic curve for unsaturated soil. J Rock Mech Geotech 132(2):131–142

Ma G, Bui HH, Lian Y, Tran KM, Nguyen GD (2022) A five-phase approach, SPH framework and applications for predictions of seepage-induced internal erosion and failure in unsaturated/saturated porous media. Comput Method Appl M 401:115614

Müller L (1964) The rock slide in the Vajont valley. Rock Mech Eng Geol 2:148–212

Müller L (1968) New considerations on the Vaiont slide. Rock Mech Eng Geol 6:1–91

Ozbay A, Cabalar AF (2015) FEM and LEM stability analyses of the fatal landslides at Çöllolar open-cast lignite mine in Elbistan, Turkey. Landslides 12:155–163

Paronuzzi P, Rigo E, Bolla A (2013) Influence of filling–drawdown cycles of the Vajont reservoir on Mt. Toc Slope Stab Geomorphol 191:75–93

Paronuzzi P, Bolla A, Rigo E (2016) Brittle and ductile behavior in deep-seated landslides: learning from the Vajont experience. Rock Mech and Rock Eng 49(6):2389–2411

Qi S, Vanapalli SK (2015) Hydro-mechanical coupling effect on surficial layer stability of unsaturated expansive soil slopes. Comput Geotech 70:68–82

Qi S, Vanapalli SK (2016) Influence of swelling behavior on the stability of an infinite unsaturated expansive soil slope. Comput Geotech 76:154–169

Segui C, Rattez H, Veveakis M (2020) On the stability of deep–seated landslides. The cases of Vaiont (Italy) and Shuping (Three Gorges Dam, China). J G Res-Earth 125(7):e2019JF005203

Selli R, Trevisan L (1964) Caratteri e interpretazione della Frana del Vaiont. Giorn Geol 32:7–104

Tang M, Xu Q, Yang H, Li S, Iqbal J, Fu X, Huang X, Cheng W (2019) Activity law and hydraulics mechanism of landslides with different sliding surface and permeability in the three gorges reservoir area. China Eng Geol 260:105212

Tika TE, Hutchinson JN (1999) Ring shear tests on soil from the Vaiont landslide slip surface. Géotechnique 49(1):59–74

Wang B, Vardon PJ, Hicks MA (2018) Rainfall-induced slope collapse with coupled material point method. Eng Geol 239:1–12

Wang G, Zhao B, Wu B, Zhang C, Liu W (2023) Intelligent prediction of slope stability based on visual exploratory data analysis of 77 in situ cases. Int J Min Sci Techno 33(1):47–59

Xu Q, Peng D, Zhang S, Zhu X, He C, Qi X, Zhao K, Xiu D, Ju N (2020) Successful implementations of a real-time and intelligent early warning system for loess landslides on the Heifangtai terrace. China Eng Geol 278:105817

Yamin M, Liang RY (2010) Limiting equilibrium method for slope/drilled shaft system. Int J Numer Anal Met 34(10):1063–1075

Yi QL, Zhao NH, Liu YL (2017) Model of landslide stability calculation based on energy conservation. Rock and Soil Mechanics 38:1–10 (**in Chinese**)

Zaniboni F, Tinti S (2014) Numerical simulations of the 1963 Vajont landslide, Italy: application of 1D Lagrangian modelling. Nat Hazards 70(1):567–592

Zhang L, Shi B, Zhang D, Sun Y, Inyang HI (2020) Kinematics, triggers and mechanism of Majiagou landslide based on FBG real-time monitoring. Environ Earth Sci 79(9):1–17

Zhou JW, Lu PY, Yang YC (2017) Reservoir landslides and its hazard effects for the hydropower station: a case study. Workshop on world landslide forum. Springer, Cham, pp 699–706